



THE UNIVERSITY *of* EDINBURGH

Edinburgh Research Explorer

## Centrifuge modelling of seepage through tailings embankments

**Citation for published version:**

Beckett, C, Fourie, AB & O'Loughlin, CD 2016, 'Centrifuge modelling of seepage through tailings embankments' International journal of physical modelling in geotechnics, vol. 16, no. 1, pp. 18-30. DOI: 10.1680/jphmg.14.00045

**Digital Object Identifier (DOI):**

[10.1680/jphmg.14.00045](https://doi.org/10.1680/jphmg.14.00045)

**Link:**

[Link to publication record in Edinburgh Research Explorer](#)

**Document Version:**

Peer reviewed version

**Published In:**

International journal of physical modelling in geotechnics

**General rights**

Copyright for the publications made accessible via the Edinburgh Research Explorer is retained by the author(s) and / or other copyright owners and it is a condition of accessing these publications that users recognise and abide by the legal requirements associated with these rights.

**Take down policy**

The University of Edinburgh has made every reasonable effort to ensure that Edinburgh Research Explorer content complies with UK legislation. If you believe that the public display of this file breaches copyright please contact [openaccess@ed.ac.uk](mailto:openaccess@ed.ac.uk) providing details, and we will remove access to the work immediately and investigate your claim.



# Centrifuge modelling of seepage through tailings embankments

C.T.S. Beckett<sup>a</sup>, A.B. Fourie<sup>a</sup>, C.D. O’Loughlin<sup>b</sup>

<sup>a</sup>*School of Civil, Environmental and Mining Engineering, University of Western Australia, 35 Stirling Highway, Crawley, WA 6009.*

<sup>b</sup>*Centre for Offshore Foundation Systems, University of Western Australia, 35 Stirling Highway, Crawley, WA 6009.*

---

## Abstract

Tailings Storage Facilities (TSFs) are manmade geotechnical structures usually comprising a perimeter embankment, fill material (the tailings) and a water level control system. Key issues often raised in TSF operation are uncertainties surrounding likely seepage to the environment and accurate prediction of seepage surfaces for input into stability assessment. Critically, TSFs are much more complex than current numerical models conventionally assume. This paper presents techniques for investigating steady-state and drawdown seepage behaviour of TSF embankments using a fixed-beam geotechnical centrifuge. The development of experimental equipment for centrifuge testing is described and novel methods to preliminarily characterise model materials, using a “desktop” centrifuge, presented. Good agreement is found between experimental results from the fixed-beam centrifuge and those predicted by the GeoStudio SEEP/W software package for steady-state and drawdown conditions at all tested hydraulic gradients.

*Keywords:* centrifuge, tailings storage facility, seepage, drawdown

---

---

*Email addresses:* [christopher.beckett@uwa.edu.au](mailto:christopher.beckett@uwa.edu.au) (C.T.S. Beckett),  
[andy.fourie@uwa.edu.au](mailto:andy.fourie@uwa.edu.au) (A.B. Fourie), [conleth.oloughlin@uwa.edu.au](mailto:conleth.oloughlin@uwa.edu.au) (C.D. O’Loughlin)

*Preprint submitted to Elsevier*

*August 3, 2015*

## 1 1. Introduction

2 It is becoming increasingly difficult to obtain a permit for a new mining op-  
3 eration. One of the abiding concerns is the ‘social licence to operate’, and key  
4 issues often raised in this regard are uncertainty surrounding seepage predictions  
5 for Tailings Storage Facilities (TSFs) for input into stability assessment. It might  
6 be considered that seepage through a TSF is now a completely tractable problem.  
7 However, this is not the case. During tailings deposition, distinct layering often  
8 occurs, as shown by numerous piezocone field testing programmes (Williams and  
9 Jones, 2005). Some of these layers may be relatively thin, but have a dispropor-  
10 tionate effect on the seepage regime (Chang et al., 2011). Furthermore, hydraulic  
11 conductivities ( $k_{sat}$ ) often decrease with depth due to consolidation (Edraki et al.,  
12 2014). These effects alone can result in reduced seepage rates to the environment  
13 and have sometimes been used as justification for the omission of an underliner.

14 Use of commercially available software to analyse seepage through TSFs is  
15 now relatively commonplace. Elegant pre-processing and finite element mesh re-  
16 finement techniques are widely available. It is also possible, to a limited extent, to  
17 account for heterogeneous tailings parameters, such as anisotropic permeability.  
18 The problem remains as to how the relevant parameters may be accurately and  
19 routinely measured. It is therefore necessary to generate experimental data that  
20 can be used to verify any numerical code, including those that will be produced  
21 in the future. There are unfortunately no analytical solutions available for the  
22 conditions described above that would enable their verification and calibration.

23 Geotechnical centrifuge modelling is now a well-established technique for in-  
24 vestigating soil behaviour (Madabhushi, 2014). However, relatively few studies  
25 have used this technique to investigate seepage phenomena in earthen embank-

26 ments. Al-Hussaini et al. (1981) presented results for seepage-induced failure of  
27 coal-waste embankments, and Cargill and Ko (1983) and Sutherland and Rechar  
28 (1984) investigated seepage through homogeneous, trapezoidal earthen embank-  
29 ments to determine phreatic surfaces under steady-state seepage and rapid draw-  
30 down of an upstream reservoir. Resnick and Znidarčić (1990) used a similar  
31 approach to these works to investigate the influence of horizontal drains on homo-  
32 geneous slope stability. More recently, Raisinghani and Viswanadham (2011) and  
33 Rajabian et al. (2012) employed centrifuge testing to investigate seepage through  
34 homogeneous embankments using various geosynthetic reinforcement techniques.  
35 These studies all used pressure measurement, digital image correlation (DIC)  
36 and/or particle image velocimetry (PIV), to identify total head levels and the  
37 position of the phreatic surface during testing. However, all encountered diffi-  
38 culties when comparing experimental results to numerical analyses, due to the  
39 creation of complex seepage flow regimes, highlighting inherent challenges in cen-  
40 trifuge testing. This paper presents the development of experimental equipment  
41 designed to address these difficulties. Scaling factors necessary for seepage analy-  
42 sis using a geotechnical centrifuge are introduced and the equipment development  
43 process described. An experimental programme is then presented for testing  
44 steady-state and drawdown seepage flow through a homogeneous embankment,  
45 where results are compared to predictions made using the GeoStudio SEEP/W  
46 software package (Geo-Slope International). Novel tests for the preliminary ma-  
47 terial characterisation are also discussed.

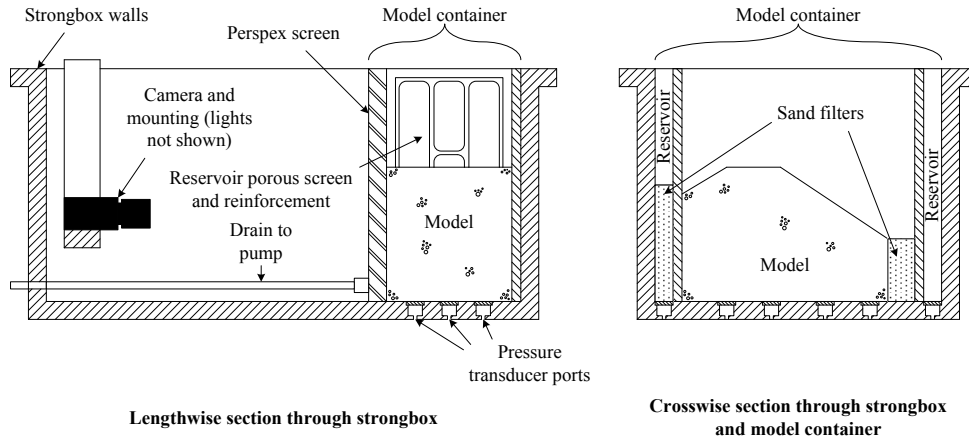


Figure 1: Sectional views through centrifuge strongbox showing principal equipment components and model container

48 **2. Equipment development**

49 *2.1. Model container*

50 The equipment used in this investigation was based on that used by Suther-  
 51 land and Rechar (1984) and Resnick and Znidarčić (1990) comprised a model  
 52 container housed within a centrifuge “strongbox”, as shown in Figure 1. The  
 53 assembled strongbox is shown in Figure 2 and an isometric view of the isolated  
 54 model container in Figure 3.

55 (Insert Figure 1 somewhere near here)

56 (Insert Figure 2 somewhere near here)

57 (Insert Figure 3 somewhere near here)

58 The model container comprises a central compartment and two flanking reser-  
 59 voirs, separated from the model by porous screens. O-rings were used to prevent  
 60 seepage around component edges or into the main strongbox. The screens pre-  
 61 vent particles from entering the reservoirs whilst allowing water to flow into or  
 62 out of the model freely. Screens were made from a layer of porous polyethylene

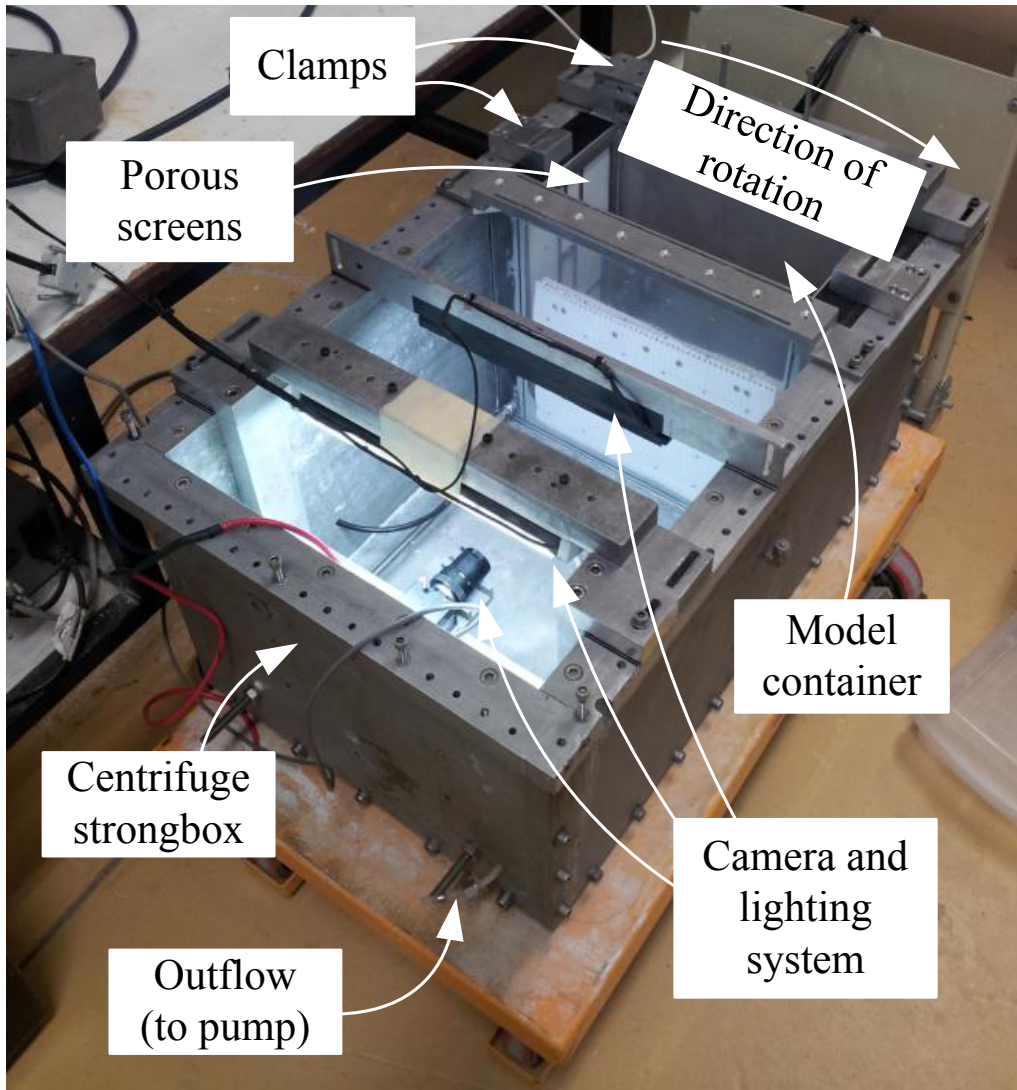


Figure 2: Centrifuge strongbox with installed model container, camera and lighting system

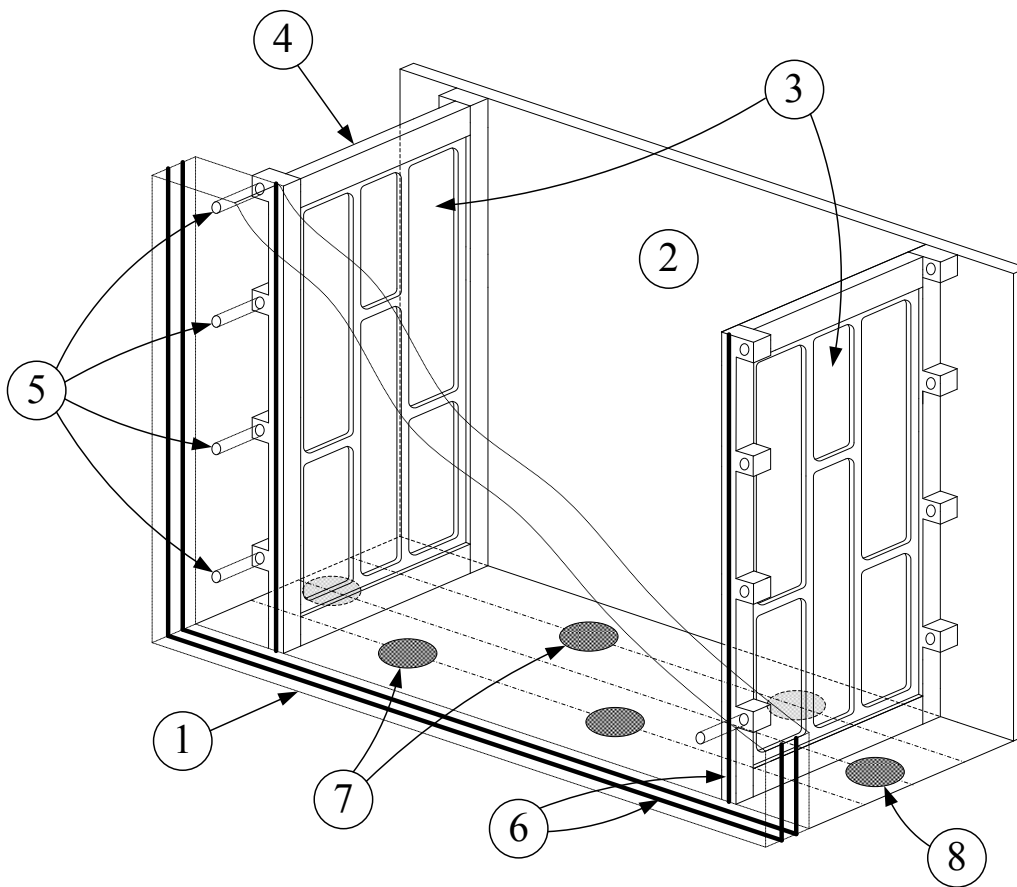


Figure 3: Model container: schematic view and components. 1) Perspex screen; 2) backing plate; 3) porous polyethylene sheets; 4) porous screen frames; 5) bolt holes; 6) O-rings; 7) embankment PPTs (under filters); 8) reservoir PPTs (under filters).

63 (pore size  $35\mu\text{m}$ ), held between a 2mm-thick stainless steel reinforcing grid. An  
64 advantage of the use of polyethylene is that sheets can easily be replaced if they  
65 become contaminated. The model container was separated from the remainder  
66 of the strongbox by a 25mm thick Perspex screen (item 1 in Figure 3), into  
67 which markers were embedded to provide a grid of known, fixed coordinates.  
68 The use of a Perspex screen allows reservoir fill and phreatic surface levels to be  
69 observed during testing. A 5 Megapixel camera (AVT Prosilica GC2450C, Fig-  
70 ure 1) was mounted within the strongbox to capture images for future DIC/PIV  
71 calculations. The lens can be locked so that the aperture and focus do not unin-  
72 tentionally change in-flight (Stanier and White, 2013).

73 Pore pressures within the model during testing were measured using four  
74 pressure transducers (PPTs), mounted in the strongbox base and protected by  
75  $\text{\O}25\text{mm}$  sintered bronze filters, as shown in section in Figure 1 and in more  
76 detail in Figure 3. PPTs were positioned to lie between the lines of porous  
77 screen reinforcement to ensure uninterrupted flow (see Figure 3). PPTs were  
78 also installed in the reservoir bases to monitor water levels during testing.

## 79 *2.2. Pumping system*

80 A number of studies including Sutherland and Rechar (1984) and Resnick  
81 and Znidarčić (1990) used overflows in upstream (U/S) and downstream (D/S)  
82 reservoirs to control water levels during testing. Flow rates through the model  
83 were assumed to equal the flow rate into the U/S reservoir. This is a robust  
84 method to ensure consistent water levels, a further advantage of which is that  
85 excess water is immediately removed from the centrifuge strongbox, preventing  
86 unbalance. However, for mine tailings, consolidation following deposition will  
87 result in the expulsion of pore water and so additional (and variable) D/S flow.



88 Therefore, the simplifying assumption that the rate of injection equals the seepage  
89 flow rate is not appropriate.

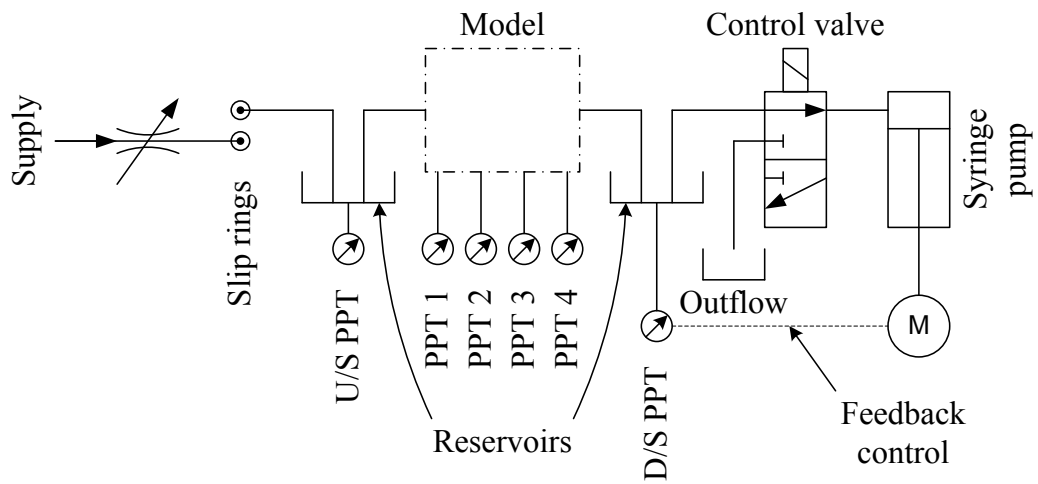
90 In this work, D/S water level was maintained by a custom-built syringe pump  
91 (internal  $\varnothing$ 50mm, 200mm stroke, maximum displacement rate 6.5mm/s, maxi-  
92 mum drive pressure 2MPa). The rate of pumping (i.e. the rate of displacement of  
93 the syringe) was controlled by an automated process where the syringe actuator  
94 was continually adjusted in a closed loop using the analogue signal from the D/S  
95 reservoir PPT; if the water level increased, the pumping rate increased to com-  
96 pensate to reestablish the target value. As the stroke and volume of the syringe  
97 are known, the flow rate out of the model can easily be calculated from the syringe  
98 displacement rate. The use of a pump allowed any D/S water level to be selected;  
99 a significant advantage over the use of a fixed overflow, enabling multiple model  
100 geometries to be accommodated. The pumping system's hydraulic configuration  
101 is shown in Figure 4, where symbols have been selected to be consistent with  
102 those used in Shepley and Bolton (2013).

103 (Insert Figure 4 somewhere near here)

### 104 **3. Experimental programme**

#### 105 *3.1. Model geometry and centrifuge scaling laws*

106 Different scaling factors must be applied to different properties to relate their  
107 values in a centrifuge model to those in the full-scale prototype. A summary  
108 of similitude laws for centrifuge seepage testing is given in Table 1. For this  
109 investigation, geometric and dynamic similarity were achieved by setting  $\lambda = \frac{1}{n}$   
110 where  $\lambda$  and  $n$  are the length and acceleration ratios between the model and the  
111 prototype. A scale factor of  $n = 100$  was used for the tests considered here, where



Legend:




- 
Pressure transducer
- 
Syringe pump actuator
- 
Variable flow rate valve

Figure 4: Container hydraulic diagram

Table 1: Summary of scaling factors for centrifuge seepage modelling assuming geometric and dynamic similitude.  $X^* = \frac{X_m}{X_p}$  where  $X_m$  and  $X_p$  are the property values in the model and prototype respectively. †At steady state

Property	Scaling factor
<b>Model parameters</b>	
Acceleration, $g^*$	$n$
Length, $\lambda$	$\frac{1}{n}$
<b>Soil parameters</b>	
Angle of friction, $\phi'^*$	1
Apparent cohesion, $c'^*$	1
Soil density, $\rho^*$	1
<b>Seepage parameters</b>	
Effective stress†, $\sigma'^*$	1
Hydraulic conductivity, $k^*$	1
Hydraulic gradient, $i^*$	$n$
Pore pressure†, $u^*$	1
Seepage velocity, $q^*$	$n$
Seepage flow rate, $Q^*$	$\frac{1}{n}$
Time (kinematic), $\tau$	$n$
Time (seepage phenomena), $t^*$	$\frac{1}{n^2}$

112  $n$  is set at the centre of the model base. This value was used following the work  
 113 of Al-Hussaini et al. (1981) to avoid potential turbulent seepage flows within the  
 114 model.

115 (Insert Table 1 somewhere near here)

116 The shape chosen for the model was typical of TSF embankments (see Fig-  
 117 ure 5); a shallow slope was included on the U/S side to represent the tailings  
 118 pond. It should be noted that the lateral extents of prototype-scale TSFs are  
 119 much greater than the 37m half-width tested here; a realistic half-width would  
 120 be of the order of 500m. However, it was necessary to select a truncated profile  
 121 in order to fit the model within the strongbox whilst testing a sensible range of  
 122 reservoir head levels.

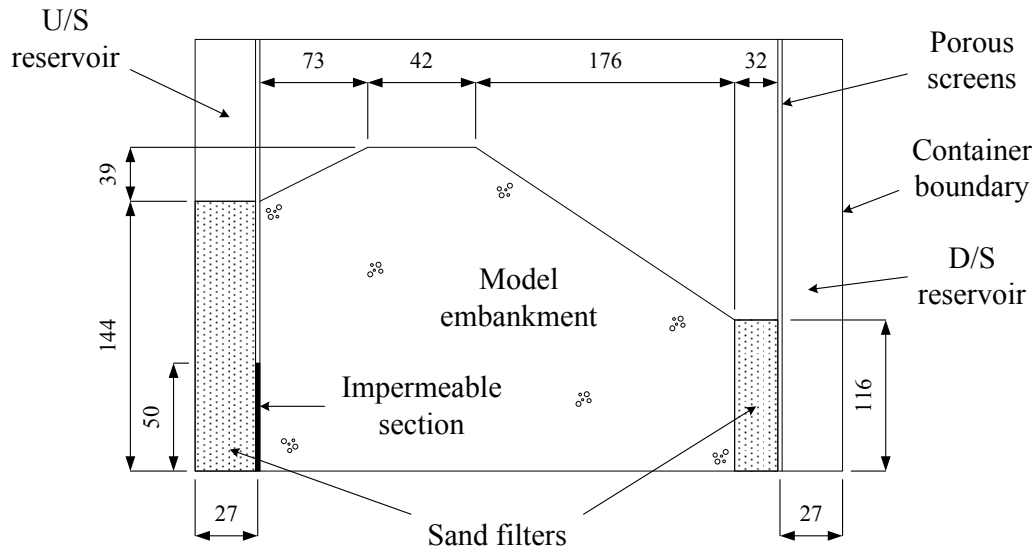


Figure 5: Model dimensions (not to scale)

123 (Insert Figure 5 somewhere near here)

124 *3.2. Material selection*

125 Although tailings are a distinctly heterogenous material, testing in this inves-  
 126 tigation was conducted on homogeneous models in order to validate the devel-  
 127 oped experimental procedures. Silica silt (Unimin Silica 200G) was selected for  
 128 the main body of the embankment, selected as preliminary testing indicated its  
 129 hydraulic conductivity to be sufficiently low to keep flow rates within the limits  
 130 of the pumping system when tested at  $n = 100$ .

131 Sand filters (shown in Figures 1 and 5) were used to prevent silt particles  
 132 migrating into and blocking the porous screens during testing. FEMA (2011)  
 133 guidelines showed that Unimin RC sand would be a suitable filter material. Silt  
 134 and sand particle grading curves, as well as the FEMA filter limits, are shown in  
 135 Figure 6.

136 (Insert Figure 6 somewhere near here)

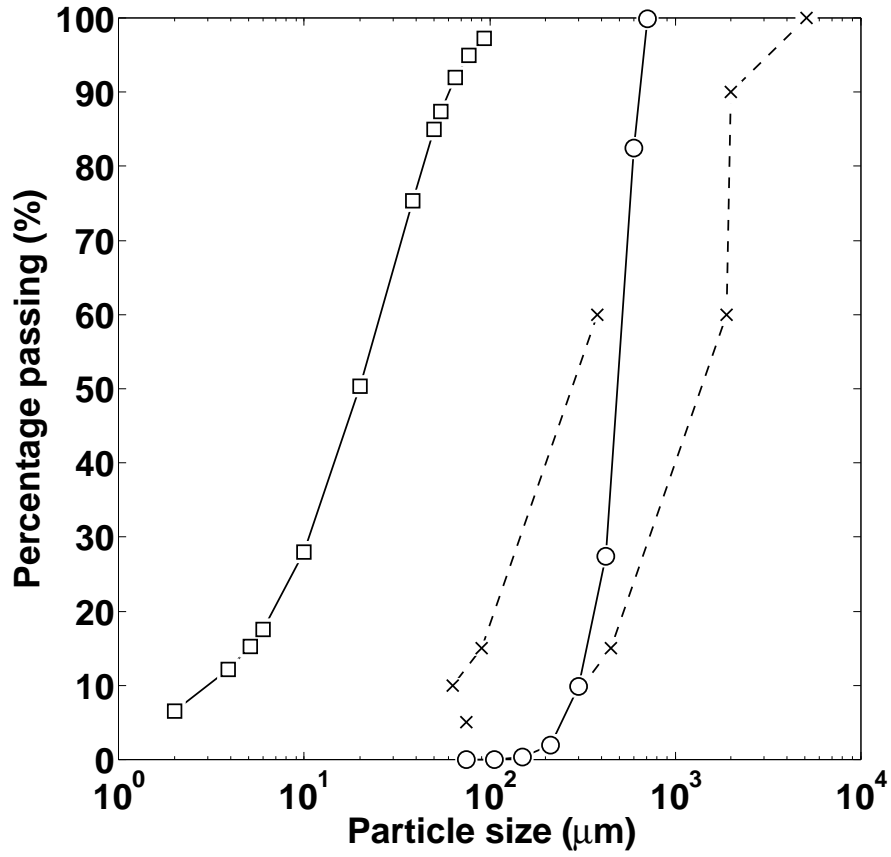


Figure 6: Embankment and filter material particle grading curves.  $\square$  RC sand;  $\circ$  Silt;  $\times$  FEMA (2011) filter limits

Table 2: Silt and sand material properties

Property	Symbol	Silt	Sand
Void ratios (-):	$e$	Figure 8	0.52
	$e_{min}$	Figure 8	0.47
	$e_{max}$	Figure 8	0.74
Particle sizes (mm):	$d_{10}$	0.003	0.299
	$d_{60}$	0.031	0.496
Specific gravity (-)	$G_s$	2.65	2.65

137 (Insert Table 2 somewhere near here)

### 138 3.3. Silt consolidation

139 A small customised desktop centrifuge, shown in Figure 7, was used to deter-  
140 mine silt consolidation properties, following the work of Kayabali and Ozdemir  
141 (2012) and Reid et al. (2012). The desktop centrifuge is a modified Clements  
142 model Orbital 420, commonly used for medical centrifugation. It is equipped with  
143 four customised sample canisters, with internal dimensions  $\text{Ø}42\text{mm} \times 92\text{mm}$ . The  
144 desktop centrifuge can spin at speeds of up to 3500RPM, allowing for a maxi-  
145 mum acceleration  $n = 2400$  at a radius of 175mm, coincident with the base of  
146 the canister (Reid et al., 2012). The desktop centrifuge is sufficiently small to  
147 be operated for extended periods without the need for specialised facilities. The  
148 advantage of this technique over a typical oedometer or Rowe cell is that multiple  
149 effective stress states can be examined in a single sample, due to the variation in  
150  $n$  with rotation radius.

151 (Insert Figure 7 somewhere near here)

152 Consolidation behaviour of the silt was determined by accelerating four sam-  
153 ples of silt slurry (at approximately 100% water content by mass) with initial  
154 sample heights of 72mm to  $n = 100$  (at the canister base) for 24 hours. A  
155 customised reaming tool (Reid et al., 2012) was used to remove 2mm slices of  
156 consolidated material at specific depths (and so effective stress levels), which were  
157 then oven dried to determine their water contents and void ratios. Results are  
158 shown in Figure 8. Note that only results for two of the four tested samples  
159 are shown in Figure 8 for clarity. Silt void ratios reach a minimum value of 0.7  
160 for effective stresses above 3kPa, indicating that the majority of the silt forming  
161 the model embankment is of homogeneous void ratio and so permeability. Such

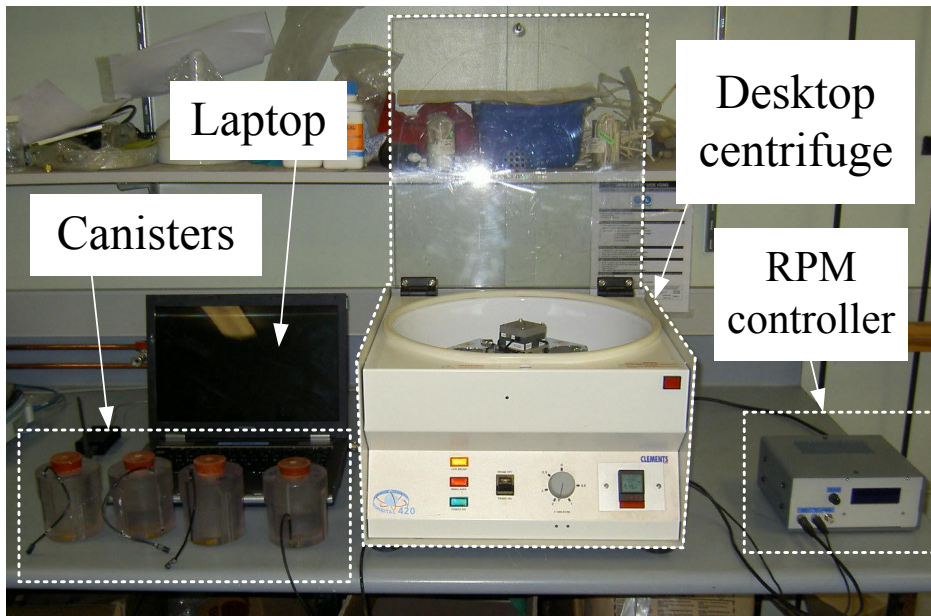


Figure 7: Desktop centrifuge with laptop, customised containers and RPM controller

162 behaviour is associated with a maximum packing density for the silt particles due  
163 to its largely uniform particle size (Figure 6).

164 (Insert Figure 8 somewhere near here)

### 165 3.4. Filter integrity: Desktop centrifuge and image analysis

166 Given the importance of the sand filters to porous screen integrity, it was  
167 necessary to test the ability of the sand filters (Figure 5) to prevent fine parti-  
168 cle migration. Testing was conducted using the desktop centrifuge. Centrifuge  
169 canisters were filled with a layer of silt slurry, poured over a layer of RC sand.  
170 Canisters were then accelerated to  $n = 100$  for a period of 7 days, allowing silt  
171 to migrate into the underlying sand under gravity. Whilst it is acknowledged  
172 that there is no seepage flow in the canister, migration is still possible due to the  
173 varying gravitation field.

174 The reaming tool could not be used to determine the extent of silt migra-  
175 tion into the sand as it was not possible to obtain incremental samples from the  
176 sand layer. An image-based technique was therefore devised to non-intrusively  
177 examine the extent of silt migration, a summary of which is shown in Figure 9.  
178 Images of the side wall of each canister were taken from a fixed distance us-  
179 ing an 8 Megapixel digital camera. An identically-sized section, corresponding  
180 to the interface region between the materials, was then cropped from each im-  
181 age (150×300 pixels). The variation in pixel intensity in each of the red, blue  
182 and green channels was then analysed. To account for any changes in lighting  
183 conditions between samples, pixel intensities were normalised using

$$I' = \frac{I - I_{min}}{I_{max} - I_{min}} \quad (1)$$

184 where  $I_{max}$  and  $I_{min}$  are the maximum and minimum intensities found in the



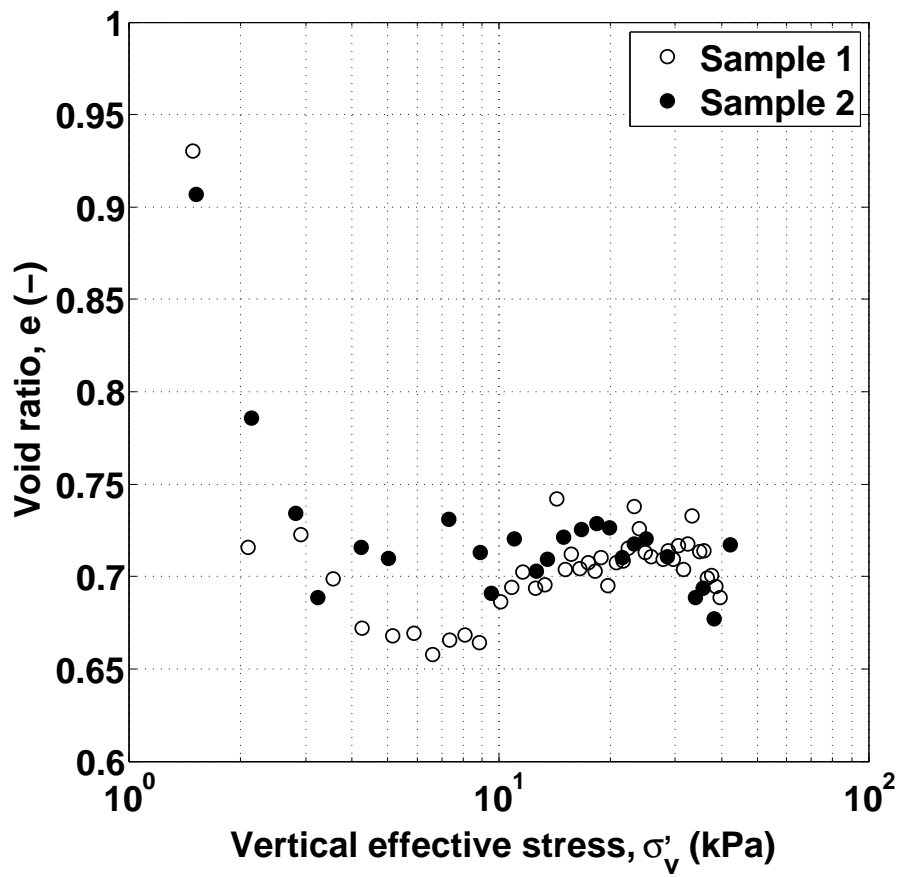


Figure 8: Silt consolidation as determined using the desktop centrifuge

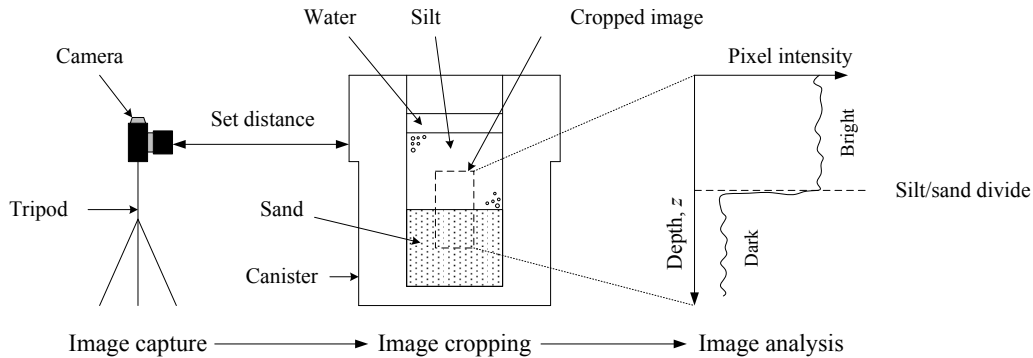


Figure 9: Process used for filter integrity testing

185 image and  $I'$  is the normalised pixel intensity value. Using Eqn 1, the brightest  
 186 pixel intensities (i.e. white) equal 1 whilst the darkest (i.e. black) equal 0.

187 (Insert Figure 9 somewhere near here)

188 Results for four tested silt-sand samples are shown in Figure 10, where depths  
 189 have been determined directly from the captured images. Note that results in  
 190 Figure 10 are for the blue channel only, as this provided the greatest contrast  
 191 between materials. A clear discontinuity in pixel intensity is visible between  
 192 depths of 19 to 25mm, corresponding to the transition between lighter silt and  
 193 darker sand particles. Also evident in Figure 10 is an increase in pixel intensity  
 194 from 0 to 19mm. Although darker intensities might suggest the presence of sand,  
 195 this feature is instead due to shadowing from the canisters' rims; no sand was  
 196 found above the layer interface. The transition depth of 6mm between the two  
 197 materials in Figure 10 suggests that a minimum filter width of 6mm is required  
 198 to prevent particle migration. Given that seepage flow was not present in the  
 199 desktop centrifuge canisters, a final filter thickness of 32mm was selected to ensure  
 200 that the porous screens remained uncontaminated.

201 (Insert Figure 10 somewhere near here)

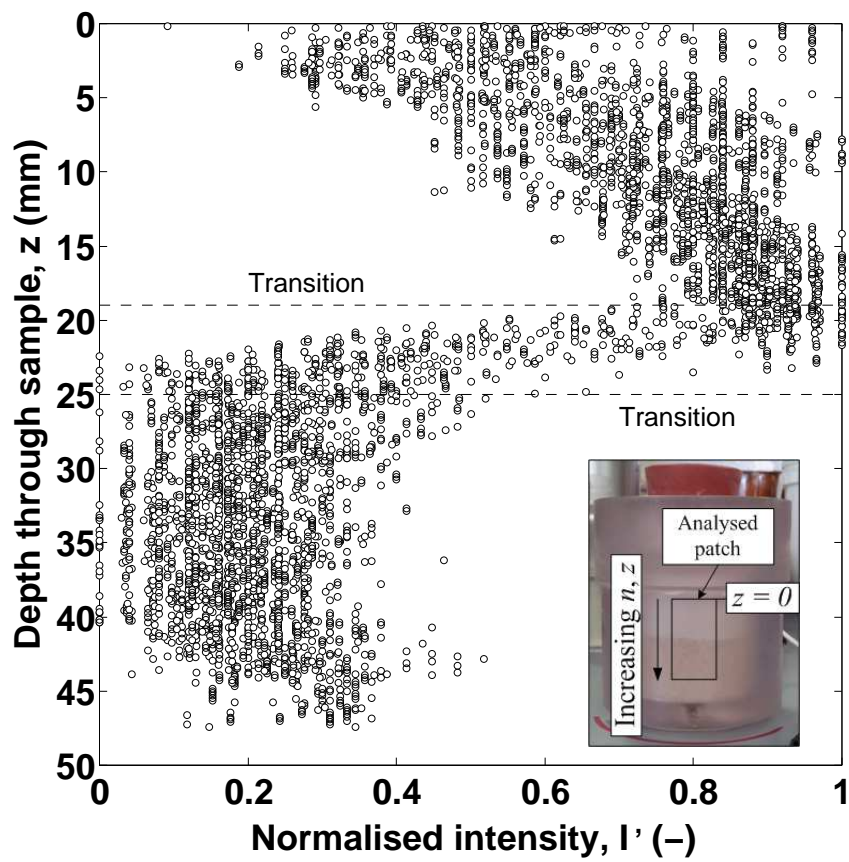


Figure 10: Normalised pixel intensities against depth (results for every 10<sup>th</sup> pixel only for clarity). Inset: Example photograph showing analysed cropped image section.

202 *3.5. Model construction*

203 The embankment and toe filter were constructed by pouring silt slurry (roughly  
204 30% water content by mass) and dry sand either side of a temporary plastic di-  
205 vider. Dry sand was deposited at a relative density of 90% by pluviation through  
206 air. U/S and D/S reservoir water levels were maintained above those of the fill  
207 during construction to prevent seepage from the model into the U/S reservoir  
208 (which might cause blockage) and to saturate the sand filter. Sand was also  
209 poured into the U/S reservoir to act as a support for the porous screen during  
210 testing. Sand was not used in the D/S reservoir to avoid migration of particles  
211 into the pumping system. The plastic divider was slowly removed once the fill  
212 reached the required depth, and water levels increased to inundate the entire  
213 model. The model was then consolidated in the centrifuge at  $n = 100$  for 24  
214 hours, after which the water level was reduced and the embankment formed by  
215 profiling the silt to create the required geometry (Figure 5).

216 *3.6. Steady-state seepage and drawdown testing*

217 Steady-state seepage conditions are representative of those present in the TSF  
218 embankment during normal operations, where tailings are deposited as a slurry  
219 within the facility and water levels are controlled by the ponding systems. Steady-  
220 state seepage testing was conducted by selecting a constant D/S reservoir level (at  
221 a depth below the surface of the sand filter) and raising the U/S reservoir water  
222 level above that value. The U/S reservoir water level was maintained at that  
223 level until steady-state seepage conditions were achieved (as demonstrated by  
224 the container PPTs), a process that took approximately 2 hours. The U/S water  
225 level was then increased to the next testing value. This process was repeated until  
226 ponding was observed on the U/S embankment slope. Flow to the U/S reservoir

227 was then terminated and water levels allowed to reduce until equilibrium was  
228 re-established with the D/S reservoir level, simulating reservoir “drawdown” at  
229 the closure of a TSF. The entire testing cycle was then repeated for a different  
230 set of target U/S reservoir water levels.

#### 231 **4. Head level calculations**

##### 232 *4.1. PPT responses*

233 The pore pressure response for one complete testing cycle (i.e. a series of  
234 U/S reservoir height increases followed by drawdown) are shown in Figure 11.  
235 An example extracted section of these data, corresponding to a period of steady-  
236 state seepage, is shown in Figure 12, where linear regression lines have been added  
237 to the data to demonstrate that steady-state conditions were achieved. It is noted  
238 that regressions fitted to measured PPT responses have negligible, rather than  
239 zero, gradients. However, pressure gradients in Figure 12 correspond to pressure  
240 variations of no greater than 0.25kPa over the 100s period, so that conditions  
241 were effectively steady-state.

242 Due to the use of a syringe pump, a series of spikes can be seen in the PPT  
243 responses shown in Figure 11. These are due to the emptying of the pump  
244 via the outflow (Figure 4), which resulted in a temporary increase in the D/S  
245 reservoir water level. Hence, spikes decrease in severity with distance from the  
246 D/S reservoir and increase in magnitude with increasing hydraulic gradients due  
247 to higher flow rates. Care was therefore taken to avoid emptying the pump  
248 towards the end of an equilibration period, to prevent erroneous readings. A  
249 large spike is seen in Figure 11 at roughly 7600s; this was due to an error in  
250 the operation of the control valve (Figure 4), resulting in the pump drawing

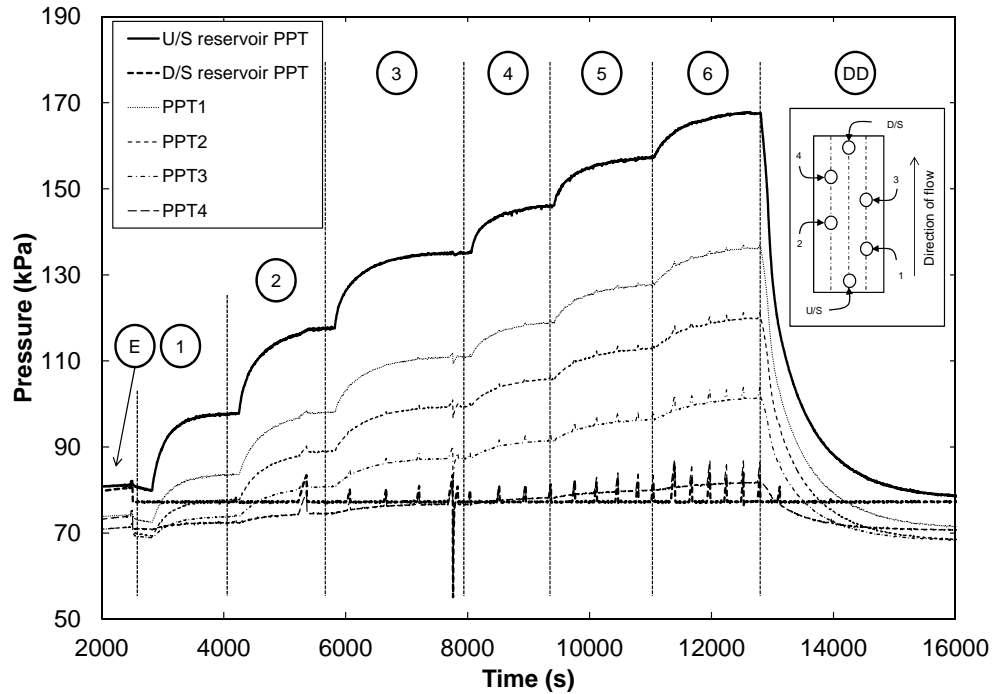


Figure 11: PPT measurements obtained during one full test cycle: E) initial equilibration; 1-6) steady-state flow equilibration periods; DD) U/S reservoir drawdown. Inset: PPT numbering and direction of flow.

251 additional water from the D/S reservoir after emptying. With the exception of  
 252 these spikes, Figure 11 shows that the syringe pump provided excellent control  
 253 over the D/S water levels for the duration of the test. This system can therefore  
 254 be used to control more complicated seepage regimes in heterogeneous materials,  
 255 e.g. tailings.

256 (Insert Figure 11 somewhere near here)

257 (Insert Figure 12 somewhere near here)

#### 258 4.2. Calculation of equivalent head levels

259 Two corrections are required to determine the position of the prototype  
 260 phreatic surface from model head levels,  $h_m$ :

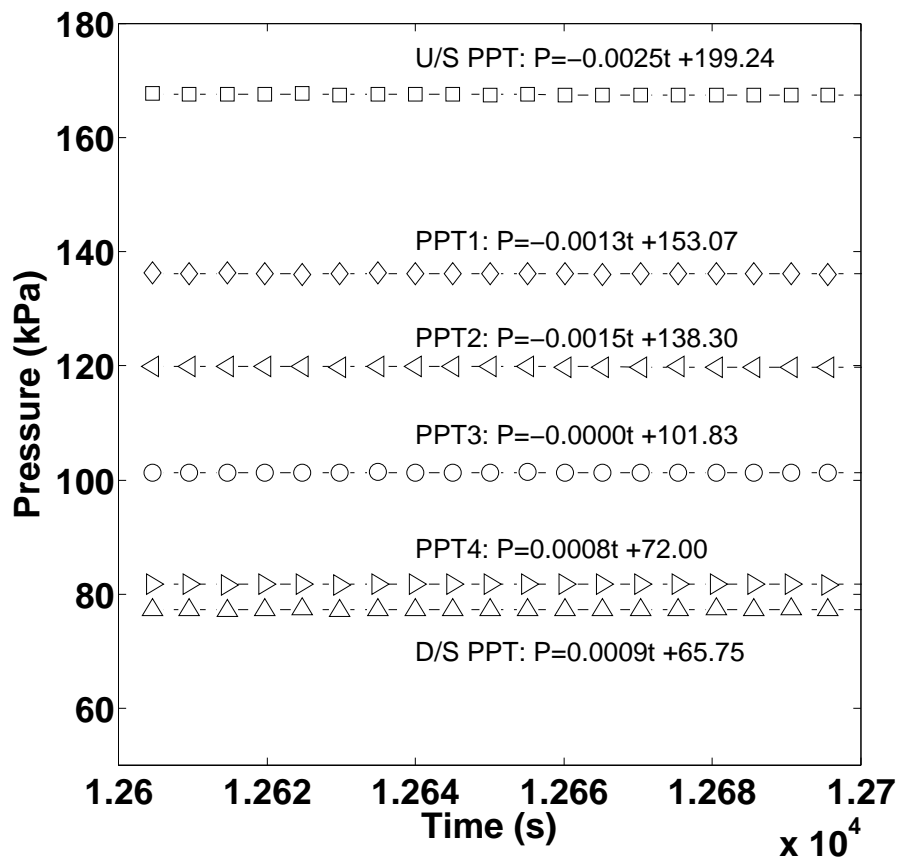


Figure 12: Example extracted PPT pressure measurements ( $P$ ) against time ( $t$ ) at steady state (data and PPT numbering as per Figure 11)

261 • Correction for the centrifuge’s radial gravitation field; PPTs detect the  
 262 pressure at the base of a water column with an axis that extends from the  
 263 point of measurement towards the centrifuge hub, rather than vertically  
 264 upwards.

265 • Correction for the average gravity acting on the water column; the gravita-  
 266 tional field varies linearly with radius from the centrifuge hub, so that the  
 267 average gravity acting on the water column also varies with its length.

268 Total model head can be calculated from measured PPT pressures,  $P$ , via

$$h_m = \frac{P}{\rho_w n_{av} g} \quad (2)$$

269 where  $\rho_w$  is the density of water at the testing temperature,  $g$  is the acceleration  
 270 due to Earth’s gravity (i.e.  $9.81 \text{ m/s}^2$ ) and  $n_{av}$  is the average acceleration scale  
 271 factor for the water column. As  $n$  varies linearly with radius from the centrifuge  
 272 hub,  $n_{av}$  is found from the average of the  $n$  values at the bottom and top of the  
 273 water column:

$$n_{bottom} = n \left( \frac{r}{R} \right) \quad (3)$$

$$n_{top} = n \left( \frac{r - h_m}{R} \right) \quad (4)$$

$$n_{av} = \frac{n}{2} \left( \frac{2r - h_m}{R} \right) \quad (5)$$

274 where  $r$  is the radius from the centre of rotation to the PPT location and  $R$  is  
 275 the radius from the hub to the base of the model along its centreline, as shown  
 276 in Figure 13. For Eqns 4 to 5,  $n = 100$  at  $R = 1760\text{mm}$  (i.e. the distance from  
 277 the centre of rotation to the model base along its centreline, as shown in Figure



278 13). Equivalent non-radial head,  $H_m$ , can then be determined via

$$H_m = h_m - (r - R) \quad (6)$$

279 Given the non-vertical orientation of the water column, the length-wise coordinate  
280 of the top of the water column (i.e. the predicted location of the phreatic surface),  
281  $X_m$ , must also be determined from the PPT lengthwise coordinate,  $x_m$ , via

$$X_m = (x_m \pm \Delta x_m) = \left( x_m \pm h_m \sin \left( \arccos \left( \frac{R}{r} \right) \right) \right) \quad (7)$$

282 where  $\Delta x_m$  is additive or subtractive depending on whether the PPT lies to  
283 the left or right of the centreline. Eqns 2 to 7 relate measured pressures to the  
284 equivalent total head at the model centreline. Hence, prototype head level,  $h_p$ ,  
285 and corresponding lengthwise coordinate of the phreatic surface,  $x_p$ , can then be  
286 found via  $h_p = nH_m$  and  $x_p = nX_m$ .

287 (Insert Figure 13 somewhere near here)

## 288 5. Steady-state behaviour

289 The software package GeoStudio 2007 SEEP/W was used to predict prototype  
290 performance, given calculated prototype U/S and D/S reservoir water levels and  
291 scaling laws provided in Table 1. Experimental and predicted results for total  
292 head levels are shown in Figures 14. Note that, as PPTs are mounted in the  
293 model container base, predicted results shown in Figure 14 are those calculated  
294 at the mesh base nodes. A comparison of experimental results and those found  
295 at these nodes is shown in Figure 15.

296 Figures 14 to 15 show good agreement between measured and predicted head

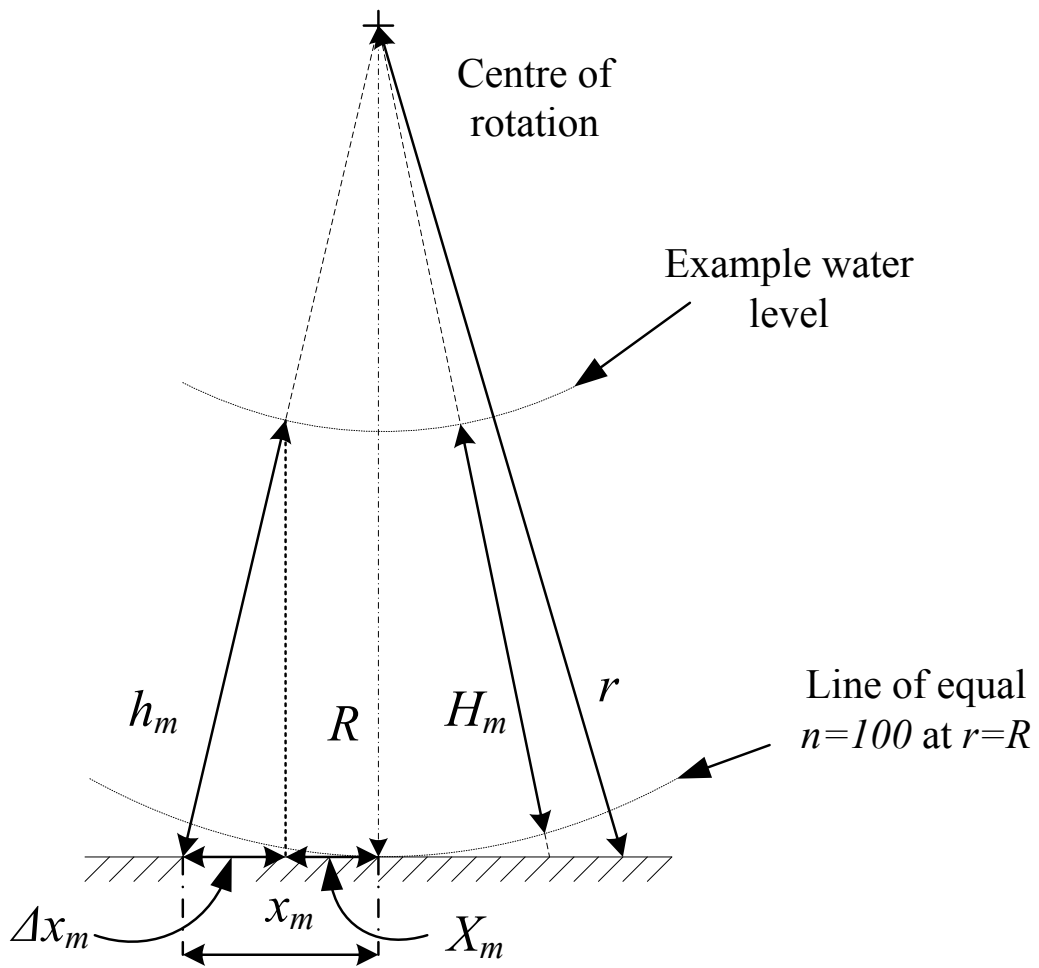


Figure 13: Conversion between model and equivalent prototype head levels.

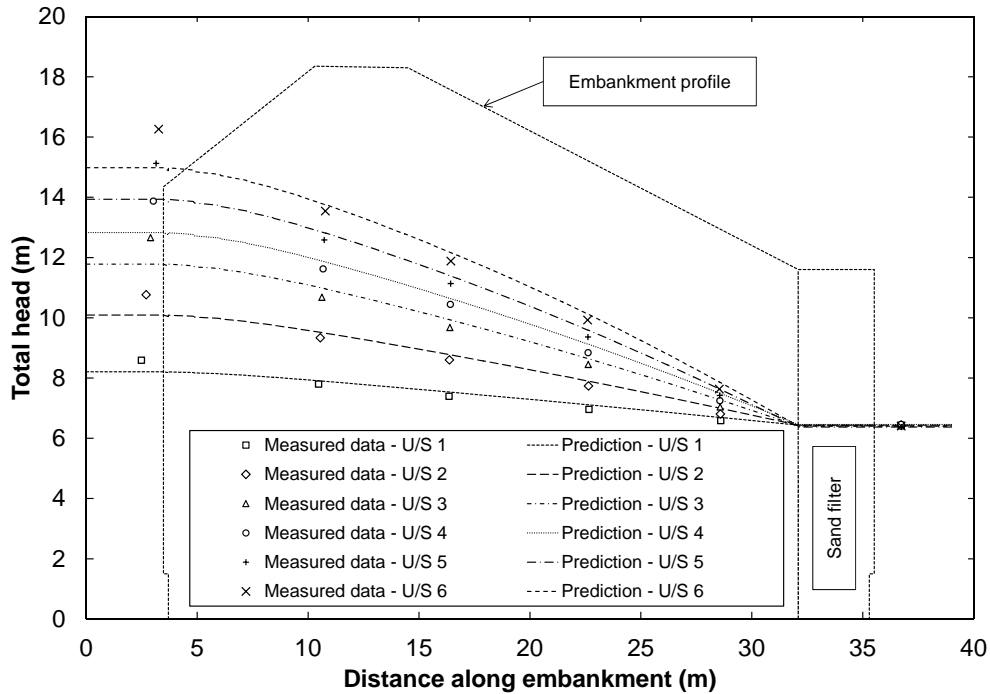


Figure 14: Example Predicted and measured results for steady-state seepage. Legend numbers correspond to U/S head increase periods shown in Figure 11.

297 values, as demonstrated in Figure 15 by results falling on or near to the line of  
 298 equality. Although it might be expected that errors would be a function of the  
 299 imposed hydraulic gradient, Figure 15 suggests that an upper error limit of 0.3m  
 300 exists for all measured head levels. It is therefore likely that this error is due to  
 301 the simplifying assumptions made in the numerical analysis, for example that no  
 302 significant head drop occurred across the U/S porous screen.

303 (Insert Figure 14 somewhere near here)

304 (Insert Figure 15 somewhere near here)

305 Notably, Figure 14 shows that predicted U/S head levels are consistently  
 306 lower (by much more than 0.3m) than those measured in the U/S reservoir. This  
 307 is unexpected, as U/S reservoir water levels were used as a boundary condition

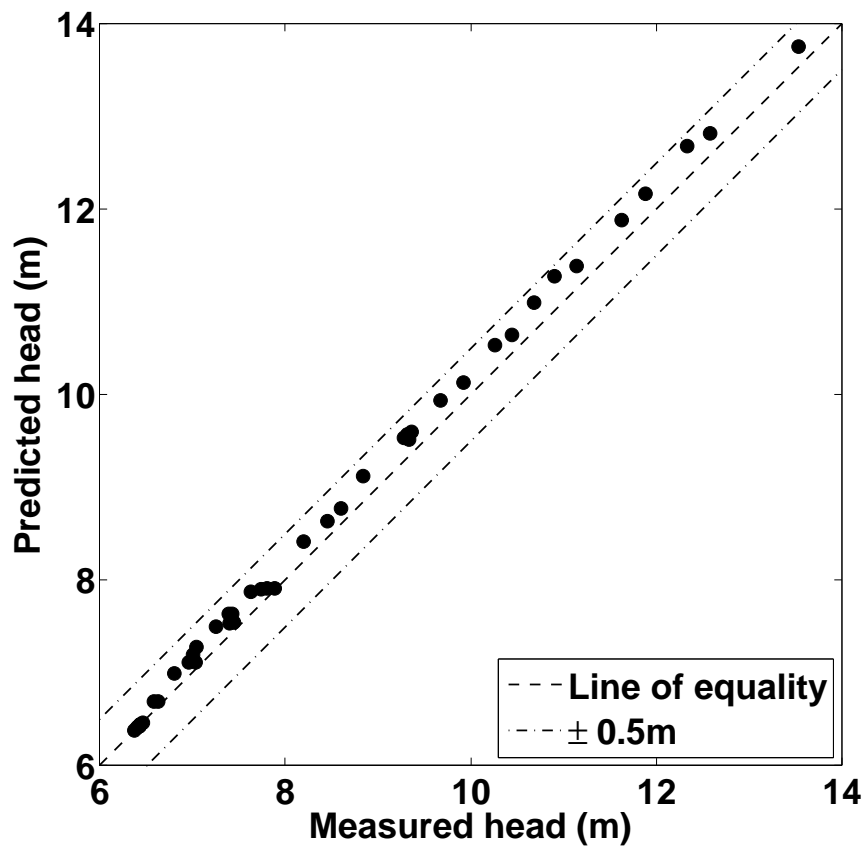


Figure 15: Predicted against measured steady-state embankment head levels for all U/S head levels (not including U/S reservoir elevations)

308 in the numerical analysis. A similar error is not seen for D/S reservoir levels,  
309 also used as a boundary condition; predicted and measured D/S head levels  
310 match. Figure 16 compares measured and predicted head levels as obtained  
311 from SEEP/W for PPT results given in Figure 12. Figure 16 shows that the  
312 predicted SEEP/W phreatic surface agrees with measured U/S and D/S values,  
313 as expected. However, the inclusion of a short impermeable section in the U/S  
314 porous screen, shown in Figure 5, results in the distortion of the equipotential  
315 lines so that they are not perpendicular to the model base. Hence, the full  
316 total head range is not detected by the base-mounted PPTs. Although a deep  
317 embankment base was used to attempt to elevate flow above this restriction, it  
318 is clear from Figure 16 that insufficient clearance was provided. A similar issue  
319 was experienced by Raisinghani and Viswanadham (2011) due to the presence of  
320 layers of geosynthetics. It is clearly essential, therefore, that seepage phenomena  
321 investigated using this technique are designed so that flow is, as far as practicable,  
322 parallel to the model base. Provided that these issues are accommodated, results  
323 shown in Figures 14 to 15 demonstrate that the experimental approach developed  
324 in this investigation can accurately reproduce steady-state seepage conditions  
325 within homogeneous embankments.

326 (Insert Figure 16 somewhere near here)

## 327 **6. Drawdown behaviour**

328 Drawdown of the U/S reservoir was modelled using transient seepage analysis  
329 in SEEP/W. Steady-state analyses were used to establish the phreatic surface,  
330 after which a reducing head boundary condition was applied to the U/S face of  
331 the reservoir, whilst maintaining a constant head level at the D/S model face.  
332 The reduction in U/S head level with time was determined directly from mea-

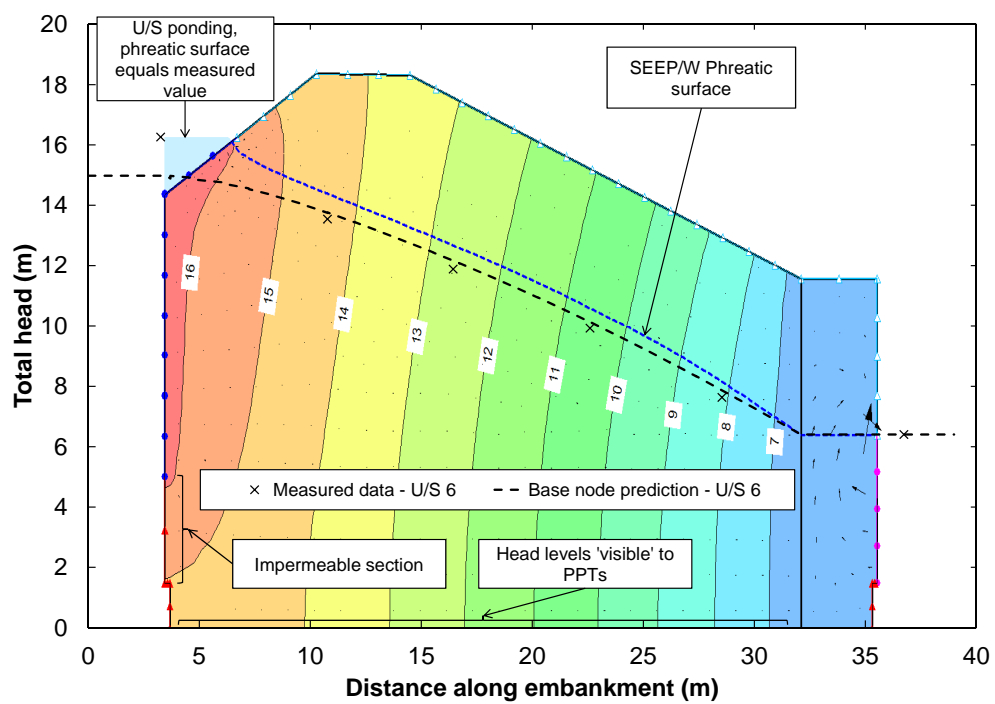


Figure 16: SEEP/W analysis for data given in Figure 12 compared to measured values (equipotential values given in m)

333 sured data for the U/S PPT, as shown in Figure 11, using an analysis period of  
334  $3.5 \times 10^7$  s.

335 As transient seepage modelling was used, estimates for material retention and  
336 hydraulic properties were required. Initial estimates for material water retention  
337 curves for silt and sand are shown in Figure 17, based on data provided in Fred-  
338 lund and Xing (1994) and known values of  $e$  (Table 2). Estimates for  $k_{sat}$  were  
339 obtained using

$$k_{sat}(\text{cm/s}) = C_0 \frac{\mu_0}{\mu_T} \left( \frac{n - 0.13}{\sqrt[3]{1 - n}} \right)^2 d_{10}^2 \quad (8)$$

340 where  $C_0 = 8$  for smooth particles,  $\frac{\mu_0}{\mu_T} = 1.3$  for testing at  $20^\circ\text{C}$ ,  $n = \frac{e}{1+e}$  and  $e$   
341 and  $d_{10}$  (in mm for use with Eqn 8) are as given in Table 2 (Terzaghi, 1925). It  
342 should be noted that the transient phreatic surface experiences increasing accel-  
343 erations, and so increasing values of  $k_{sat}$ , as its level reduces. However, as this  
344 change is small for small changes in elevation, analyses were conducted assuming  
345  $n = 100$  for all head levels.

346 (Insert Figure 17 somewhere near here)

347 Although drawdown is a transient phenomenon, negligible difference was  
348 found between analyses for variations in  $k_{sat}$  of several orders of magnitude,  
349 due to the experimentally-defined U/S boundary condition. Seepage was there-  
350 fore suggestibly sufficiently slow to be largely independent of hydraulic properties  
351 (i.e. quasi-static). Initial estimates for retention and hydraulic properties were  
352 therefore deemed sufficient for comparison to experimental data. Note that, for  
353 heterogeneous materials such as mine tailings, this simplification would not be  
354 valid and accurate retention and hydraulic conductivity functions would be re-  
355 quired.

356 Figure 18 shows example experimental and predicted results for total head

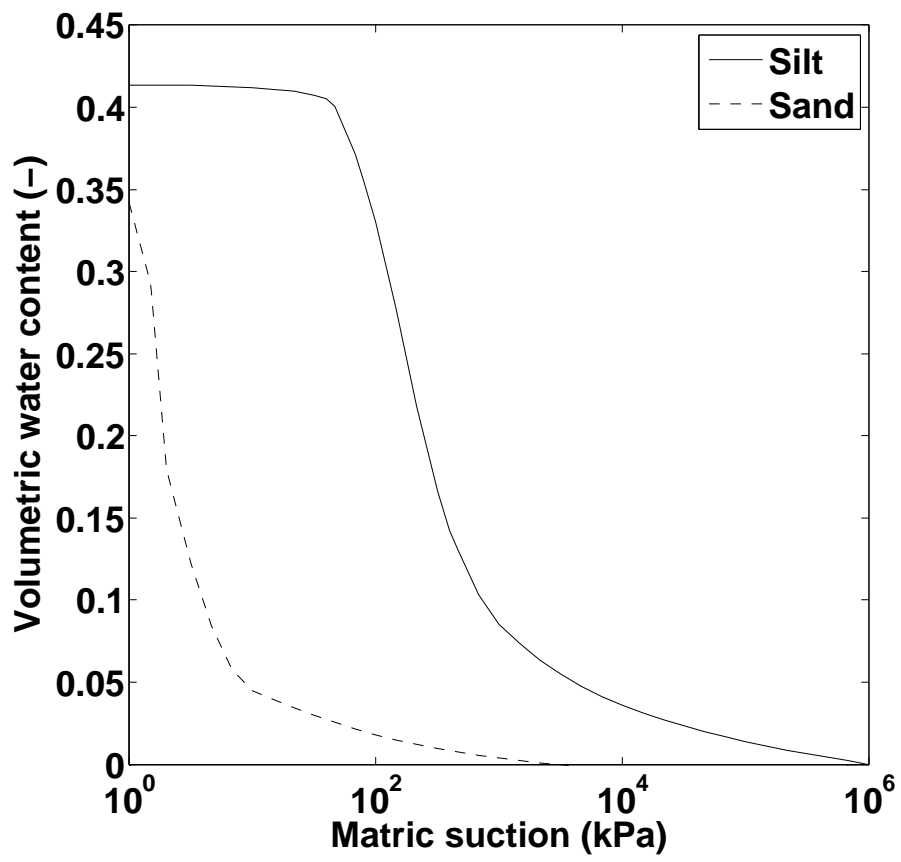


Figure 17: Estimated soil-water retention curves for silt and sand



357 levels (predicted at the embankment base) during drawdown. Predicted and  
358 experimental values are compared in Figure 19. Good agreement is seen in Fig-  
359 ure 18 between measured and predicted results throughout the embankment pro-  
360 file. This is also shown in Figure 19, where errors are within  $\pm 0.4\text{m}$  and fall  
361 evenly about the line of equality. Drawdown was largely complete after 3200s,  
362 equivalent to roughly 370 days at  $n = 100$ . As discussed previously, however, the  
363 larger lateral extents of full-scale TSFs mean that drawdown times in practice  
364 are likely to be far longer than those found in this work, suggesting that pumping  
365 might be required for decades in order to fully restore groundwater equilibrium.

366 Unlike in Figure 15, both positive and negative differences are seen in Fig-  
367 ure 19. A potential cause of this error is the assumption that  $n = 100$  at all  
368 times during drawdown. Overprediction of processes dominated by horizontal  
369 flow (i.e. steady-state seepage surfaces) and underprediction of those dominated  
370 by vertical flow (i.e. reducing head levels during transient seepage) also suggests  
371 that a degree of heterogeneity existed within the embankment material, so that  
372  $k_{sat,h} > k_{sat,v}$ . This is consistent with the deposition of the silt slurry in lay-  
373 ers during model construction; although material was subsequently consolidated,  
374 preferential flow in the horizontal direction may have remained. This is an im-  
375 portant observation, as it is well-known that layered structures are also created  
376 during tailings deposition in TSFs. Scale models should therefore incorporate  
377 this layered structure in order to capture the effects of hydraulic heterogeneity  
378 on seepage performance.

379 (Insert Figure 18 somewhere near here)

380 (Insert Figure 19 somewhere near here)

381 The good agreement found between measured and predicted steady-state and  
382 drawdown results demonstrates that experimental techniques developed and em-

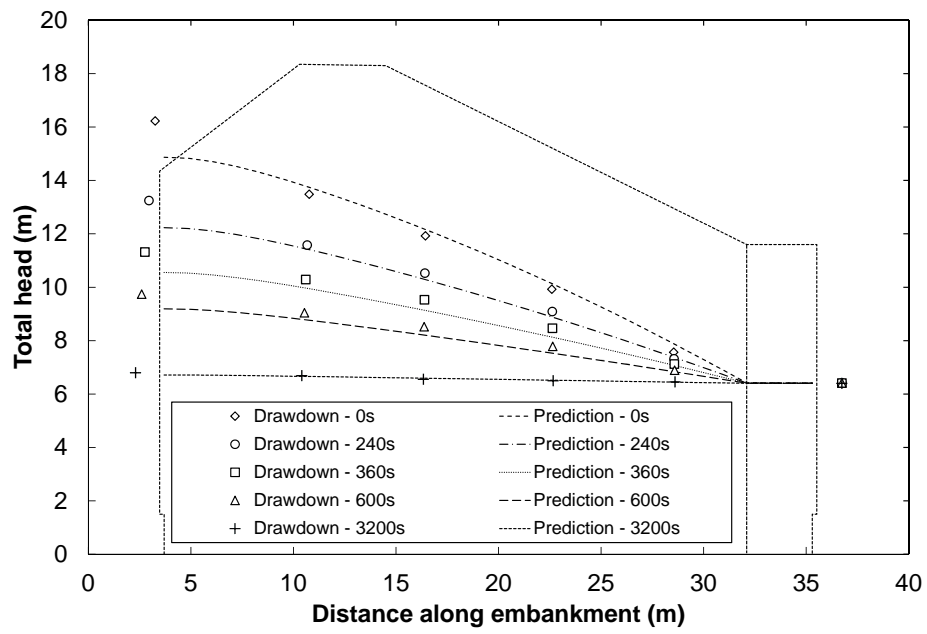


Figure 18: Example predicted and measured results for times following U/S reservoir drawdown.

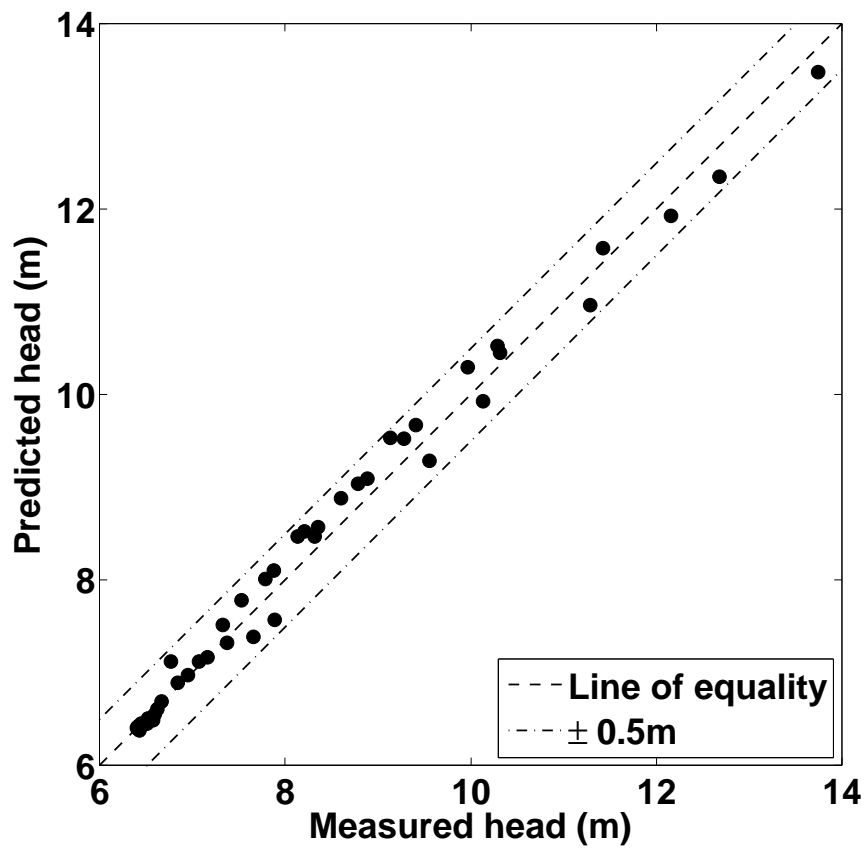


Figure 19: Predicted against measured steady-state embankment head levels for all U/S head levels during drawdown (not including U/S values)

383 ployed in this investigation are able to accurately capture embankment seepage  
384 behaviour. Notably, these techniques offer greater flexibility than those previ-  
385 ously used in terms of D/S flow rate measurement and accurate control of U/S  
386 and D/S water levels. This facility can now be used to investigate more com-  
387 plicated seepage scenarios, for example those encountered in full-scale TSFs, to  
388 provide data for improving current seepage prediction models.

## 389 **7. Conclusion**

390 Seepage conditions within TSF embankments are likely to be far more com-  
391 plicated than current models predict. There is therefore a need for experimental  
392 data against which updated numerical models can be verified. This paper has de-  
393 scribed the design and development of apparatus for measuring seepage through  
394 model TSF embankments using a geotechnical centrifuge. The use of a syringe  
395 pump was shown to be an effective method to control D/S water levels and to  
396 measure seepage flow rates. Novel processes for determining material consol-  
397 idation behaviour and sand filter effectiveness using a desktop centrifuge and  
398 image-based analysis were also described, each providing rapid alternatives to  
399 conventional testing methods.

400 Results for steady-state seepage through a homogeneous model were presented  
401 and good agreement was found between measured results and those predicted for  
402 an equivalent full-scale prototype using SEEP/W. A maximum error of 0.3m was  
403 found between measured and predicted results, which was seemingly independent  
404 of testing hydraulic gradient and attributed to assumptions made during numer-  
405 ical modelling. It was also demonstrated that flow through the model must be  
406 designed so that it is parallel to the model base if seepage behaviour is to be  
407 tested using equipment similar to that developed in this work.

408 Predicted results for changes in total head during U/S reservoir drawdown,  
409 based on simplifying quasi-steady assumptions, showed good agreement with nu-  
410 merical predictions. Differences of  $\pm 0.4\text{m}$  between measured and predicted values  
411 were similar to those found for steady-state seepage. A comparison of steady-  
412 state and drawdown experimental results suggested that these differences were  
413 due to a slight material heterogeneity developed during deposition. A drawdown  
414 time of roughly 370 days was predicted for the tested embankment profile. Based  
415 on these results, there is confidence that techniques developed here can reliably  
416 reproduce seepage conditions within full-scale heterogeneous embankments.

## 417 **8. Acknowledgements**

418 The authors would like to gratefully acknowledge funding awarded from The  
419 Integrated Tailings Management Project, funded through AMIRA International  
420 by; Anglo American, Freeport McMoran, Gold Fields, Total E&P Canada, New-  
421 mont, Shell Canada Energy, BASF, Nalco and Outotec.

## 422 **9. References**

- 423 Al-Hussaini, M. M., Goodings, D. J., Schofield, A. N., Townsend, F. C., 1981. Centrifuge mod-  
424 eling of coal waste embankments. *Journal of the Geotechnical Engineering Division* 107,  
425 481–499.
- 426 Cargill, K., Ko, H., 1983. Centrifugal modeling of transient water flow. *J. Geotech. Engrg.*  
427 109 (4), 536–555.
- 428 Chang, N., Heymann, G., Clayton, C., 2011. The effect of fabric on the behaviour of gold  
429 tailings. *Géotechnique* 61, 187–197.
- 430 Edraki, M., Baumgartl, T., Manlapig, E., Bradshaw, D., Franks, D. M., Moran, C. J., 2014.  
431 Designing mine tailings for better environmental, social and economic outcomes: a review of  
432 alternative approaches. *Journal of Cleaner Production* in press.

433 FEMA, 2011. Filters for embankment dams: Best practices for design and construction. Tech.  
434 rep., Federal Emergency Management Agency.

435 Fredlund, D. G., Xing, A., 1994. Equations for the soil-water characteristic curve. *Canadian*  
436 *Geotechnical Journal* 31, 521–532.

437 Kayabali, K., Ozdemir, A., 2012. Assessing the practicality of the centrifuge method for 1-d  
438 consolidation. *Bulletin of Engineering Geology and the Environment* 71 (4), 735–745.

439 Madabhushi, G., 2014. Centrifuge modelling for civil engineers. CRC Press, UK.

440 Raisinghani, D., Viswanadham, B., 2011. Centrifuge model study on low permeable slope rein-  
441 forced by hybrid geosynthetics. *Geotextiles and Geomembranes* 29, 567–580.

442 Rajabian, A., Viswanadham, B., Ghiassian, H., Salehzadeh, H., 2012. Centrifuge model studies  
443 on anchored geosynthetic slopes for coastal shore protection. *Geotextiles and Geomembranes*  
444 34, 144–157.

445 Reid, D., Fourie, A., Watson, S., 16–19 April 2012. Accelerated consolidation testing of slurries  
446 using a desktop centrifuge. In: Jewell, R., Fourie, A., Paterson, A. (Eds.), *Proceedings of*  
447 *the 15th International Seminar on Paste and Thickened Tailings (PASTE 2012)*. Australian  
448 Centre for Geomechanics, Sun City, South Africa, pp. 43–52.

449 Resnick, G. S., Znidarčić, D., 1990. Centrifugal modeling of drains for slope stabilization. *Journal*  
450 *of Geotechnical Engineering* 116 (11), 1607–1624.

451 Shepley, P., Bolton, M. D., 2013. Water supply to a geotechnical centrifuge. *International Journal*  
452 *of Physical Modelling in Geotechnics* 13, 99–110.

453 Stanier, S. A., White, D. J., 2013. Improved image-based deformation measurement in the  
454 centrifuge environment. *Geotechnical Testing Journal* 36, 1–14.

455 Sutherland, H., Rechar, R., 1984. Centrifuge simulations of stable tailings dam. *J. Geotech.*  
456 *Engrg.* 110 (3), 390–402.

457 Terzaghi, K., 1925. Principles of soil mechanics. *Engineering News Records* 95 (19, 742–746; 20,  
458 796–800; 21, 832–836; 22, 874–878; 23, 912–915; 25, 987–990; 26, 1026–1029; 27, 1064–1068).

459 Williams, D., Jones, H., 2005. Tailings storage facilities. In: Wills, B. A. (Ed.), *Advances in*  
460 *Gold Ore Processing*. Vol. 15 of *Developments in Mineral Processing*. Elsevier, Amsterdam,  
461 The Netherlands, Ch. 30, pp. 729–752.

462 Figure captions:

- 463 1. Sectional views through centrifuge strongbox showing principal equipment  
464 components and model container
- 465 2. Centrifuge strongbox with installed model container, camera and lighting  
466 system
- 467 3. Model container: schematic view and components. 1) Perspex screen; 2)  
468 backing plate; 3) porous polyethylene sheets; 4) porous screen frames; 5)  
469 bolt holes; 6) O-rings; 7) embankment PPTs (under filters); 8) reservoir  
470 PPTs (under filters).
- 471 4. Container hydraulic diagram
- 472 5. Model dimensions (not to scale)
- 473 6. Embankment and filter material particle grading curves.  $\square$  RC sand;  $\circ$  Silt;  
474  $\times$  FEMA (2011) filter limits
- 475 7. Desktop centrifuge with laptop, customised containers and RPM controller
- 476 8. Silt consolidation as determined using the desktop centrifuge
- 477 9. Process used for filter integrity testing
- 478 10. Normalised pixel intensities against depth (results for every 10<sup>th</sup> pixel only  
479 for clarity). Inset: Example photograph showing analysed cropped image  
480 section.
- 481 11. PPT measurements obtained during one full test cycle: E) initial equi-  
482 libration; 1-6) steady-state flow equilibration periods; DD) U/S reservoir  
483 drawdown. Inset: PPT numbering and direction of flow.
- 484 12. Example extracted PPT pressure measurements ( $P$ ) against time ( $t$ ) at  
485 steady state (data and PPT numbering as per Figure 11)
- 486 13. Conversion between model and equivalent prototype head levels.

- 487 14. Example Predicted and measured results for steady-state seepage. Legend  
488 numbers correspond to U/S head increase periods shown in Figure 11.
- 489 15. Predicted against measured steady-state embankment head levels for all  
490 U/S head levels (not including U/S reservoir elevations)
- 491 16. SEEP/W analysis for data given in Figure 12 compared to measured values  
492 (equipotential values given in m)
- 493 17. Estimated soil-water retention curves for silt and sand
- 494 18. Example predicted and measured results for times following U/S reservoir  
495 drawdown.
- 496 19. Predicted against measured steady-state embankment head levels for all  
497 U/S head levels during drawdown (not including U/S values)

498 Table captions:

- 499 1. Summary of scaling factors for centrifuge seepage modelling assuming ge-  
500 ometric and dynamic similitude.  $X^* = \frac{X_m}{X_p}$  where  $X_m$  and  $X_p$  are the  
501 property vales in the model and prototype respectively. †At steady state
- 502 2. Silt and sand material properties